

1 **A direct comparison between field-measured**
2 **and sensor-based estimates of soil carbon**
3 **dioxide flux across six National Ecological**
4 **Observatory Network sites enabled by the**
5 **neonSoilFluxR package**neonSoilFlux: An R

6 Package for Continuous Sensor-Based
7 Estimation of Soil CO₂ Fluxes

8 John Zobitz¹ Ed Edward Ayres² Zoey Werbin³
9 Ridwan Abdi¹ Natalie Ashburner-Wright⁴ Lillian Brown⁴
10 Ryan Frink-Sobierajski⁴ Lajntxiag Lee¹ Dijonë Mehmeti¹
11 Christina Tran⁴ Ly Xiong¹ Naupaka Zimmerman^{4,5}

12 ¹ Augsburg University, 2211 Riverside Avenue, Minneapolis, MN 55454

13 ² National Ecological Observatory Network, Battelle, 1685 38th Street, Suite 100, Boulder, CO
14 80301

¹⁵ ³ Boston University, 5 Cummington Street, Boston, MA 02215

¹⁶ ⁴ University of San Francisco, 2130 Fulton Street, San Francisco, CA 94117

¹⁷ ⁵ University of Kansas, 1450 Jayhawk Boulevard, Lawrence, KS 66045

¹⁸ **Acknowledgments**

¹⁹ JZ acknowledges Kathleen O'Rourke for code development. NZ thanks technical staff at
²⁰ USF for support with field gear assembly and shipping. We thank the NEON field staff and
²¹ assignable assets teams for facilitating each of the six NEON site visits. We are grateful to
²² LI-COR technical staff for helpful discussions about optimal soil chamber sampling methods.

²³ This work was supported by NSF DEB grant #2017829 awarded to JZ, and NSF DEB grant
²⁴ #2017860 awarded to NZ. This material is based in part upon work supported by the National
²⁵ Ecological Observatory Network (NEON), a program sponsored by the U.S. National Science
²⁶ Foundation (NSF) and operated under cooperative agreement by Battelle. We also thank the
²⁷ reviewers and subject editor for their constructive feedback.

²⁸ **Conflict of Interest Statements**

²⁹ None of the authors have a financial, personal, or professional conflict of interest related to this
³⁰ work.

³¹ **Author Contributions**

³² Conceptualization: JZ, NZ; Methodology: EA, JZ, NZ; Software: JZ, NZ, ZW, E A, DM, RA,
³³ LX, LL; Validation: JZ, NZ; Formal Analysis: JZ, NZ, DM, RA, LX, LL; Investigation: JZ, NZ,

³⁴ RF-S, CT, NA-W, LB; Resources: JZ, NZ; Data curation: JZ, NZ, DM, LX; Writing – original
³⁵ draft: JZ, NZ; Writing – review and editing: JZ, NZ, ZW, EA, CT, DM, LX,; Visualization: JZ,
³⁶ NZ, DM, RA, LX; Supervision: JZ; NZ; Project Administration: JZ; NZ; Funding Acquisition:
³⁷ JZ; NZ

³⁸ **Data Availability**

³⁹ ~~Data available~~ Anonymous field-collected data, neonSoilFlux calculated outputs, and
⁴⁰ manuscript-generating code for peer review are provided as supplemental files. All will
⁴¹ be made available via Zenodo prior to publicly available on Zenodo with a DOI upon
⁴² publication.

43 **1 Abstract**

44 A key component of constraining the uncertainty Accurate quantification of soil carbon fluxes
45 is essential to reduce uncertainty in estimates of the terrestrial carbon sink is quantification
46 of terrestrial soil carbon fluxes, which vary across time and ecosystem type. One method for
47 the estimation of these fluxes and their associated uncertainties is the flux gradient method,
48 which can be calculated via a variety of existing approaches. Robust estimation of . However,
49 these fluxes vary over time and across ecosystem types and so it can be difficult to estimate
50 them accurately across large scales. The flux gradient method estimates soil carbon fluxes on a
51 sub-daily level requires using co-located measurements of soil CO₂ concentration, water content,
52 temperature, and other environmental measurements and soil temperature, soil moisture, and
53 other soil properties. These data are publicly available from the The National Ecological
54 Observatory Network at sites spanning a range of (NEON) provides such data across 20 different
55 ecoclimatic domains across the continental United States ecoclimatic domains spanning the
56 continental U.S., Puerto Rico, Alaska, and Hawai'i. We present an R software package
57 (`neonSoilFlux`) that acquires NEON soil environmental data and computes soil carbon flux
58 at a half-hourly time step at a user-specified NEON site and month in a tidy data format.
59 To validate to compute half-hourly soil carbon fluxes for each soil replicate plot at a given
60 terrestrial NEON site. To assess the computed fluxes, we visited six focal NEON sites and
61 measured soil carbon fluxes using a closed-dynamic chamber approach. The validation confirmed
62 that a primary challenge in reducing soil carbon flux uncertainty is correctly characterizing
63 diffusivity and soil water content across the soil profile. Outputs from the `neonSoilFlux`
64 package showed order-of-magnitude agreement to measured fluxes (R^2 between measured and
65 `neonSoilFlux` outputs ranging from 0.00 to 0.78); measured outputs fell within the range
66 of calculated uncertainties from the gradient method. Calculated fluxes from `neonSoilFlux`
67 aggregated to the daily scale exhibited expected site-specific seasonal patterns. While the

68 flux gradient method is broadly effective, its accuracy is highly sensitive to site-specific inputs,
69 particularly estimates of soil diffusivity and moisture content. Future refinement and validation
70 of `neonSoilFlux` outputs can contribute to existing databases of soil carbon flux measurements,
71 providing near real-time estimates of a critical component of the terrestrial carbon cycle.

72 **1.1 Keywords**

73 Soil carbon, carbon dioxide, flux gradient, carbon cycle, field validation, soil respiration,
74 ecosystem variability, diffusion

75 **2 Data for peer review**

76 Anonymous ~~data and field-collected data, neonSoilFlux calculated outputs, and manuscript-generating~~
77 code for peer review ~~is available here:~~ [LINK](#) ~~are provided as supplemental files. All will be~~
78 ~~made publicly available on Zenodo with a DOI upon publication.~~

79 **3 Introduction**

80 Soils contain the planet's largest reservoir of terrestrial carbon (Jobbágy & Jackson, 2000). A
81 critical component of this reservoir is soil organic matter, the accumulation of which is influenced
82 by biotic factors such as above-ground plant inputs (Jackson et al., 2017). These inputs in
83 turn are influenced by environmental factors such as growing season length, temperature, and
84 moisture (Desai et al., 2022), which also affect the breakdown of soil organic matter and its
85 return to the atmosphere. Across heterogeneous terrestrial landscapes, the interplay between
86 these biotic and abiotic factors influence the size of the soil contribution to the terrestrial carbon

87 sink (Friedlingstein et al., 2023~~2025~~). However, the heterogeneity of these processes across
88 diverse ecosystems in the context of rapid environmental change leads to large uncertainty
89 ~~in about~~ the magnitude of this sink in the future, and thus ~~there remains~~ a pressing need to
90 quantify changes in soil carbon pools and fluxes across scales.

91 Ecological observation networks such as the United States' National Ecological Observatory
92 Network (NEON) and others (e.g. ~~the globally-distributed~~ FLUXNET or the ~~European~~ Inte-
93 grated Carbon Observation System) present a significant advancement in the nearly continuous
94 observation of biogeochemical processes at the continental scale. Notably, at 47 terrestrial
95 sites across the continental United States ~~that span 20 ecoclimatic domains~~, NEON provides
96 half-hourly measurements of soil CO₂ concentration, temperature, and moisture at different
97 vertical depths. Each of these NEON sites also encompasses measurements of the cumulative
98 sum of all ecosystem carbon fluxes in an airshed using the eddy covariance technique (Balocchi,
99 2014). Soil observations provided by NEON are on the same timescale and standardized with
100 eddy covariance measurements from FLUXNET. These types of nearly continuous observational
101 data (NEON and FLUXNET) can be used to reconcile differences between model-derived
102 or data-estimated components of ecosystem carbon flux (Jian et al., 2022; Luo et al., 2011;
103 Phillips et al., 2017; J. Shao et al., 2015; P. Shao et al., 2013; Sihi et al., 2016).

104 Estimated or observed soil carbon fluxes are a key metric for understanding change in soil
105 carbon pools over time (Bond-Lamberty et al., 2024). A soil carbon flux to the atmosphere (F_S ,
106 units $\mu\text{mol m}^{-2} \text{s}^{-1}$), represents the aggregate process of transfer of soil CO₂ to the atmosphere
107 from physical and biological processes (e.g. diffusion and respiration). Soil carbon fluxes can
108 be assumed to encompass soil carbon respiration from autotrophic or heterotrophic sources
109 (Davidson et al., 2006) ~~, typically assumed to be static across the soil biome~~ and modeled with
110 a exponential Q_{10} paradigm (Bond-Lamberty et al., 2004; Chen & Tian, 2005; Hamdi et al.,
111 2013).

112 One common method by which F_S is measured in the field is through the use of soil chambers
113 in a closed, well-mixed system (Norman et al., 1997) with headspace trace gas concentra-
114 tions measured with an infrared gas analyzer (IRGA). F_S can also be estimated from soil
115 CO_2 measurements at different depths in the soil using the flux-gradient method (Maier &
116 Schack-Kirchner, 2014). This method is Closed-chamber IRGA measurements, while being the
117 most common method, require either frequent in-person site visits or expensive and fragile
118 automated systems. The potential of the gradient method is that fluxes can be estimated
119 from continuous data recorded by robust solid-state sensors. The flux-gradient method is
120 an approach that uses conservation of mass to calculate flux at a vertical soil depth z at steady state
121 by applying Fick's law of diffusion. A simplifying assumption for the flux-gradient method is
122 that there is no mass transfer in the other spatial dimensions x and y (Maier & Schack-Kirchner,
123 2014). The diffusivity profile, a key component of this calculation, varies across the soil depth
124 as a function of soil temperature, soil volumetric water content, atmospheric air pressure, and
125 soil bulk density (Millington & Shearer, 1971; Moldrup et al., 1999; Sallam et al., 1984).

126 Databases such as the Soil Respiration Database (SRDB) or the Continuous Soil Respiration
127 Database (COSORE) add to the growing network of resources for making collected observations
128 of soil fluxes available to other workers researchers (Bond-Lamberty, 2018; Bond-Lamberty et
129 al., 2020; Bond-Lamberty & Thomson, 2010; Jian et al., 2021; Jiang et al., 2024). However,
130 these databases currently encompass primarily direct soil measurements of fluxes (i.e. those
131 using methods like the closed-chamber method described above). Currently, NEON provides
132 all measurements to calculate F_S from Fick's law, but soil flux as a derived data product was
133 descoped from the initial network launch due to budget constraints (Berenbaum et al., 2015).
134 Deriving estimates of F_S using continuous sensor data across NEON sites thus represents
135 remains a high priority.

136 This study describes an R software package, `neonSoilFlux`, that ~~can be used to derive~~

¹³⁷ computes a standardized estimate of F_S at all terrestrial NEON sites. ~~After calculating~~
¹³⁸ ~~these flux estimates, we then validated them against using the flux-gradient method. Using~~
¹³⁹ direct chamber-based field observations of soil carbon dioxide flux from a subset of terrestrial
¹⁴⁰ NEON sites spanning six states, we provide a direct validation of F_S from neonSoilFlux.

¹⁴¹ Key objectives of this study are to:

- ¹⁴² 1. Apply the flux-gradient method to estimate soil CO₂ flux from continuous sensor mea-
¹⁴³ surements across six NEON sites.
- ¹⁴⁴ 2. Benchmark estimated soil carbon fluxes against field measurements (e.g. direct chamber
¹⁴⁵ measurements of soil flux).
- ¹⁴⁶ 3. Identify sources of error in the flux-gradient approach across diverse sites in order to
¹⁴⁷ guide future work.

¹⁴⁸ 4 Materials and Methods

¹⁴⁹ 4.1 Field methods

¹⁵⁰ 4.1.1 Focal NEON Sites

¹⁵¹ In order to acquire field data to validate model predictions of flux, we selected six terrestrial
¹⁵² NEON sites for analysis. We conducted roughly week-long field measurement campaigns at
¹⁵³ these sites, which span a range of environmental gradients and terrestrial domains (Table 1).
¹⁵⁴ SJER, SRER, and WREF were visited during May and June of 2022, and WOOD, KONZ,
¹⁵⁵ and UNDE during May and June of 2024.

156 Over the course of two field campaigns in 2022 and 2024, we conducted week-long visits at
157 each site. In consultation with NEON field staff, we first selected a specific plot in the soil
158 sampling array to maximize the concurrent availability of sensor data.

159 **4.1.2 Soil collar placement**

160 Either one (2022 sampling campaign) or two (2024 sampling campaign) PVC soil collars (20.1
161 cm inside diameter) were installed in close proximity to the permanent NEON soil sensors
162 at each site (Figure 1). ~~The soil plot where measurements were taken~~ As instruments in the
163 NEON soil sensor arrays can occasionally break down or stop working, the specific soil plot
164 where we made measurements was chosen at each site in consultation with NEON staff to
165 maximize likelihood of quality soil sensor measurements during the duration of the IRGA
166 measurements. The plot selected at each site (out of the 5 in each replicate array at each site)
167 are presented in the last column of Table 1. After installation, collar(s) were left to equilibrate
168 for approximately 24 hours prior to any measurements being taken.

169 **4.1.3 Infrared gas analyzer measurements of soil CO₂ flux**

170 In 2022, we then made measurements of flux on an hourly interval for 8 hours each day.
171 Measurements were taken from roughly 8 am to 4 pm, with the time interval selected to
172 capture the majority of the diurnal gradient of soil temperature each day. These measurements
173 were made using a LI-6800 infrared gas analyzer instrument (LI-COR Environmental, Lincoln,
174 NE) fitted with a soil chamber attachment (attachment 6800-09). In 2024, we again used the
175 same LI-6800 instrument, but made half-hourly measurements over an approximately 8 hour
176 period. In addition, in 2024 we also installed a second collar and used a second instrument, an
177 LI-870 CO₂ IRGA, connected to an automated robotic chamber (LI-COR chamber 8200-104)

178 controlled by an LI-8250 multiplexer, to make automated measurements. The multiplexer was
179 configured to take half-hourly measurements 24 hours a day for the duration of our sampling
180 bout at each site. Each instrument was paired with a soil temperature and moisture probe
181 (Stevens HydraProbe, Stevens Water, Portland, OR) that was used to make soil temperature
182 and moisture measurements concurrent with the CO₂ flux measurements. Chamber volumes
183 were set by measuring collar offsets at each site. System checks were conducted daily for the
184 LI-6800 and weekly for the LI-8250. Instruments were factory calibrated before each field
185 season.

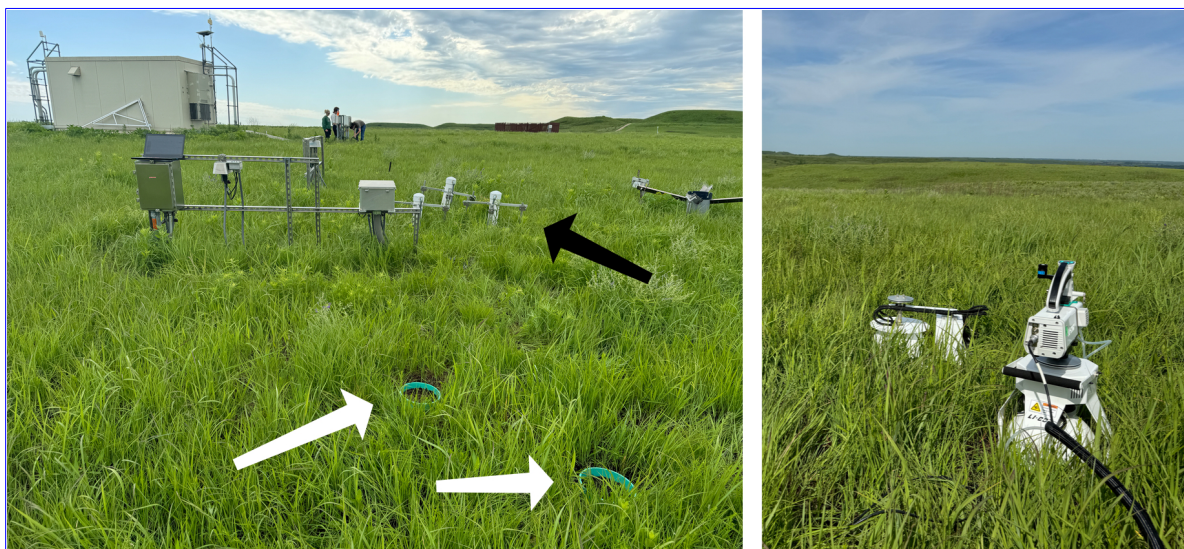


Figure 1: Spatial layout of field sampling using a closed-dynamic chamber setup at a representative NEON site (KONZ). Left image shows collars (white arrows) and permanent soil sensor installation (black arrow) and right image shows the LI-6800 (foreground) and LI-8200-104 (background) instruments placed on the collars.

g of NEON sites studied for field work and analysis. Site refers to NEON site Santa Rita Experimental Range (SRER), San Joaquin Experimental Range (SJER), Wind River Experimental Forest (WREF), Chase Lake National Wildlife Refuge (WOOD), Konza Prairie Biological Station (KONZ), and the University of Notre Dame Environmental Research Center (UNDE). Location is reported in decimal degrees of latitude and longitude. Other abbreviations include Mean Annual Temperature (MAT); T_S : average soil temperature during field measurements; SWC: average soil water content during field measurements. Soil plot Dates refer to field measurement dates for each site. Plot refers to the particular location in the soil array (denoted as HOR by NEON) where field measurements were made.

Site (NEON site ID)	Location	Ecosystem type	Mean annual	Mean annual	Field measurement	Soil plot Plot	
			MAT	T_S ($^{\circ}$ C)	MAP		
Santa Rita Experimental Range (SRER)	31.91068, -110.83549	Shrubland	19.3 °C	47.6 °C	346 mm	4.0%	004 29-May 2024-01 June 2024 May 29- June 1 2022
San Joaquin Experimental Range (SJER)	37.10878, -119.73228	Oak woodland	16.4 °C	41.7 °C	540 mm	1.2%	005 01-June 2022-04 June 1-4 2022
Wind River Experimental Forest (WREF)	45.82049, -121.95191	Evergreen forest	9.2 °C	15.3 °C	2225 mm	27.2%	001 07-June 2022-09 June 7-9 2022
Chase Lake National Wildlife Refuge (WOOD)	47.1282, -99.241334	Restored prairie grassland	4.9 °C	14.9 °C	495 mm	14.9%	001 03-June 2024-09 June 3-9 2024
Konza Prairie Biological Station (KONZ)	39.100774, -96.563075	Tallgrass prairie	12.4 °C	23.4 °C	870 mm	23.4%	001 29-May May 29- June 1 2024 -01-June 2024

g of NEON sites studied for field work and analysis. Site refers to NEON site Santa Rita Experimental Range (SRER), San Joaquin Experimental Range (SJER), Wind River Experimental Forest (WREF), Chase Lake National Wildlife Refuge (WOOD), Konza Prairie Biological Station (KONZ), and the University of Notre Dame Environmental Research Center (UNDE). Location is reported in decimal degrees of latitude and longitude. Other abbreviations include Mean Annual Temperature (MAT); T_S : average soil temperature during field measurements; SWC: average soil water content during field measurements. Soil plot Dates refer to field measurement dates for each site. Plot refers to the particular location in the soil array (denoted as HOR by NEON) where field measurements were made.

Site (NEON site ID)	Location	Ecosystem type	Mean annual temperature (MAT)	$\overline{T_S}$ (°)	Mean annual precipitation (MAP)	SWC (%)	Field measurement dates	Soil plot Plot
University of Notre Dame Environmental Research Center (UNDE)	46.23391, -89.537254	Deciduous forest	4.3 °C	13.0 °C	802 mm	13.0%	May 22–25 2024–25	004

186 4.1.4 Post-collection processing of field data

187 We used LI-COR SoilFluxPro software (v 5.3.1) to assess the data after collection and to
 188 inform sampling parameters. We checked appropriateness of dead band and measurement
 189 durations using built-in evaluation tools. Based on this, the deadband period was set for 30-40
 190 seconds, depending on the site, and the measurement duration was 180 seconds with a 30
 191 second pre-purge and a 30 second post-purge at most sites, and a 90 sec pre- and post-purge at
 192 sites with higher humidity due to recent precipitation events. We also assessed the R^2 of linear
 193 and exponential model fits to measured CO₂ to verify measurement quality.

194 **4.2 neonSoilFlux R package**

195 We developed an R package ([neonSoilFlux; LINK TO BE ADDED AFTER PEER](#)
196 [REVIEW](#))[neonSoilFlux; Zobitz et al. \(2024\)](#)) to compute half-hourly soil carbon fluxes
197 and uncertainties from NEON data. The objective of the `neonSoilFlux` package is a
198 unified workflow (Figure 2) for soil data acquisition and analysis that supplements the
199 existing data acquisition R package [neonUtilities \(LINK TO BE ADDED AFTER PEER](#)
200 [REVIEW](#))[```
graph TD; A\[Month, Year, NEON site\] --> B\[Acquire data from neonUtilities\]; B --> C\[Gap filling and QA flags\]; C --> D\[Interpolate data to same depth\]; D --> E\[Compute fluxes across layers\]; E --> F\[Soil flux, uncertainties, and QA flags\]
```

The diagram illustrates the workflow of the `neonSoilFlux` R package. It begins with an input box labeled "Month, Year, NEON site" \(orange parallelogram\). An arrow points from this box to a process box labeled "Acquire data from `neonUtilities`" \(green rectangle\). From this process, an arrow points down to another process box labeled "Gap filling and QA flags" \(blue rectangle\). From there, an arrow points left to a process box labeled "Interpolate data to same depth" \(blue rectangle\). From this box, an arrow points down to a process box labeled "Compute fluxes across layers" \(blue rectangle\). Finally, an arrow points right from this box to an output box labeled "Soil flux, uncertainties, and QA flags" \(purple parallelogram\).](https://CRAN.R-project.org/package=neonUtilities; Lunch et al. (2025)</a>.</p></div><div data-bbox=)

Figure 2: Diagram of `neonSoilFlux` R package. For a given month, year, and NEON site (orange parallelogram), the package acquires all relevant data to compute  $F_S$  using the `neonUtilities` R package (green rectangle). Data are gap-filled according to reported QA flags and interpolated to the same measurement depth before computing the soil flux, uncertainties, and final QA flags (blue rectangles). The package reports the associated soil flux, uncertainties, and quality assurance (QA) flags for the user (purple parallelogram).

201 At a given NEON [observation site](#) there are five replicate soil plots, each with measurements of

202 soil CO<sub>2</sub> concentration, soil temperature, and soil moisture at different depths (Figure 3). The  
 203 `neonSoilFlux` package acquires measured soil water content (National Ecological Observatory  
 204 Network (NEON), 2024e), soil CO<sub>2</sub> concentration (National Ecological Observatory Network  
 205 (NEON), 2024b), barometric pressure from the nearby tower (National Ecological Observatory  
 206 Network (NEON), 2024a), soil temperature (National Ecological Observatory Network (NEON),  
 207 2024d), and soil properties (e.g. bulk density) (National Ecological Observatory Network  
 208 (NEON), 2024c). The static soil properties were collected from a nearby soil pit during site  
 209 characterization and are assumed to be constant at each site. A soil flux calculation is computed  
 210 at each replicate soil plot.

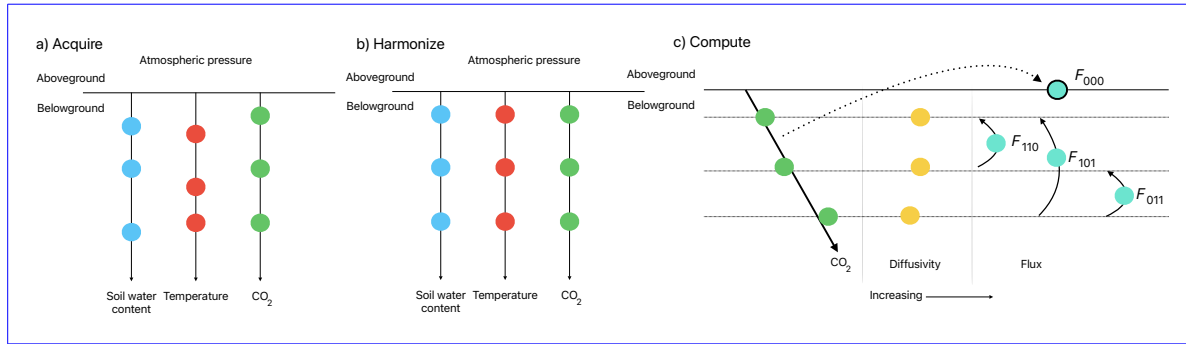


Figure 3: Model diagram for data workflow for the `neonSoilFlux` R package. a) Acquire: Data are obtained from given NEON location and horizontal sensor location, which includes soil water content, soil temperature, CO<sub>2</sub> concentration, and atmospheric pressure. All data are screened for quality assurance; if gap-filling of missing data occurs, it is flagged for the user. b) Any belowground data are then harmonized to the same depth as CO<sub>2</sub> concentrations using linear regression. c) The flux across a given depth is computed via Fick's law, denoted with  $F_{ijk}$ , where  $i$ ,  $j$ , or  $k$  are either 0 or 1 denoting the layers the flux is computed across ( $i$  = closest to surface,  $k$  = deepest).  $F_{000}$  represents a flux estimate where the gradient  $dC/dz$  is the slope of a linear regression of CO<sub>2</sub> with depth.

211 The workflow to compute a value of  $F_S$  with `neonSoilFlux` consists of three primary steps,  
 212 illustrated in Figure 3. First, NEON data are acquired for a given site and month via the  
 213 `neonUtilities` R package (yellow parallelogram and green rectangle in Figure 2 and Panel  
 214 a in Figure 3). Acquired environmental data can be exported to a comma separated value

215 file for additional analysis. Quality assurance (QA) flags are reported as an indicator variable.  
216 Since the calibration coefficients on the soil water content sensors have changed over time  
217 (National Ecological Observatory Network (NEON), 2024e), raw sensor measurements were  
218 back-calculated and soil-specific calibrations were applied following Ayres et al. (2024) to  
219 generate a consistent time series at each measurement location.

220 The second step is harmonizing the data to compute soil fluxes across soil layers. This  
221 step consists of three different actions (blue rectangles in Figure 2 and Panel b in Figure 3).  
222 If a given observation by NEON is reported as not passing a quality assurance check, we  
223 applied a gap filling method to replace that measurement with its monthly mean at that same  
224 depth (Section 4.2.1). Belowground measurements of soil water and soil temperature are then  
225 interpolated to the same depth as soil CO<sub>2</sub> measurements. The diffusivity (Section 4.2.2) and  
226 soil flux across different soil layers (Section 4.2.3) are then computed.

227 The third and final step is computing a surface soil flux through extrapolation to the sur-  
228 face (purple parallelogram in Figure 2 and Panel c in Figure 3). Uncertainty on a soil flux  
229 measurement is computed through quadrature. An aggregate quality assurance (QA) flag  
230 for each environmental measurement is also reported, representing if any gap-filled measure-  
231 ments were used in the computation of a soil flux. Within the soil flux-gradient method,  
232 several different approaches can be used to derive a surface flux (Maier & Schack-Kirchner,  
233 2014); the `neonSoilFlux` package reports four different possible values for soil surface flux  
234 (Section 4.2.3).

235 **4.2.1 Gap-filling routine**

236 NEON reports QA flags as a binary value for a given binary values for each measurement  
237 and half-hourly time interval. We replaced any flagged measurements at a location's spatial

interval. For a given half-hour, if any input variable (soil CO<sub>2</sub> concentration, soil temperature, or soil moisture) at depth  $z$  is flagged, computation of  $F_S$  is not possible. To address this, flagged measurements and their uncertainties were replaced with a bootstrapped sample of the monthly mean for all un-flagged measurements for that month. These measurements are represented by the vector monthly mean ( $\bar{m}$ ) and monthly standard deviation ( $\bar{s}$ ) (Efron & Tibshirani, 1994).

For each month, depth  $z$ , and variable, we computed bootstrapped estimates of  $\bar{m}$  and  $\bar{s}$  from the vectors of unflagged measurements ( $\mathbf{m}$ , standard errors), reported standard errors ( $\sigma$ ), and the 95% confidence interval (the so-called expanded uncertainty,  $\epsilon$ , or expanded uncertainty; Farrance & Frenkel (2012)). All of these vectors have length  $M$ . We have that  $\vec{\sigma}_i \leq \vec{c}_i$ . We define the bias as. We also defined a bias vector  $\mathbf{b} = \sqrt{\epsilon^2 - \sigma^2}$ , which quantifies the spread of uncertainty in a given period and is incorporated into  $\bar{m}$ .

We generate a vector of bootstrap samples of the distribution of the monthly mean  $\bar{m}$  and monthly standard error  $\bar{\sigma}$  the following ways:

Randomly sample from the uncertainty and bias independently:  $\sigma_j$  and the bias  $\mathbf{b}_k$  (not necessarily the same sample). Generate From these, 5000 bootstrap samples were generated for  $\mathbf{m}$ ,  $\sigma$ , and  $\mathbf{b}$ . For each sample ( $m_k, b_k, \sigma_k$ ), we generated a vector  $\mathbf{n}$  of length  $N$ , where  $\mathbf{n}_i$  is a random sample (length  $N = 5000$ ) by drawing from a normal distribution with mean  $m_i - m_k + b_k$  and standard deviation  $\sigma_j$ . Since  $M < N$ , values from  $\mathbf{m}$  will be reused. With these  $N$  random samples,  $\bar{y}_i = \bar{x} + \vec{b}_k$  and  $s_i$  is the sample standard deviation of  $\bar{x}$ . We expect that  $s_i \approx \vec{\sigma}_j$ . The reported monthly  $\sigma_k$ . The sample mean and standard deviation are then computed  $\bar{y}$  and  $\bar{s}$ . Measurements and uncertainties that did not pass the QA check are then substituted with  $\bar{y}$  and were then computed from  $\mathbf{n}$ . The resulting distributions of sample means and sample standard deviations provided the bootstrapped monthly mean ( $\bar{m}$ ) and standard error ( $\bar{s}$ ) respectively.

263 This gap-filling ~~method described here~~ procedure provides a consistent ~~approach for each~~  
264 ~~data stream, however we recognize that other gap-filling alternatives may be warranted for~~  
265 ~~longer-term treatment across all data streams. However, alternative approaches may be better~~  
266 ~~suites for longer gaps (e.g. such as, correlations with other NEON measurement levels and/or~~  
267 ~~soil plots) or measurement specific gap-filling routines or for variable-specific conditions.~~ We  
268 discuss the effect of gap-filling on our ~~measurements~~ results in Section 66.1.

269 **4.2.2 Soil diffusivity**

270 Soil diffusivity  $D_a$  at a given measurement depth is the product of the diffusivity in free air  
271  $D_{a,0}$  ( $\text{m}^2 \text{ s}^{-1}$ ) and the tortuosity  $\xi$  (no units) (Millington & Shearer, 1971).

272 We compute  $D_{a,0}$  with Equation 1:

$$D_{a,0} = 0.0000147 \cdot \left( \frac{T_i + 273.15}{293.15} \right)^{1.75} \cdot \left( \frac{P}{101.3} \right) \quad (1)$$

273 where  $T_i$  is soil temperature ( $^\circ\text{C}$ ) at depth  $i$  (National Ecological Observatory Network (NEON),  
274 2024d) and  $P$  surface barometric pressure (kPa) (National Ecological Observatory Network  
275 (NEON), 2024a).

276 Previous studies by Sallam et al. (1984) and Tang et al. (2003) demonstrated the sensitivity  
277 of modeled  $F_S$  depending on the ~~tortuosity model~~ tortuosity model ( $\xi$ ) used to compute  
278 diffusivity. At low soil water content, the choice of ~~tortuosity model may lead to order of~~  
279 ~~magnitude~~ tortuosity model can lead to order-of-magnitude differences in  $D_a$ , which in turn  
280 affect modeled  $F_S$ . The `neonSoilFlux` package ~~uses two different models for currently includes~~  
281 two approaches to calculate  $\xi$ , representing the ~~extremes~~ range of tortuosity behavior reported  
282 in Sallam et al. (1984).

283 The first approach ~~uses~~is the Millington-Quirk model ~~for diffusivity, Equation 2~~ (Millington &  
284 Shearer, 1971), in which tortuosity depends on both porosity and soil water content:

$$\xi = \frac{(\phi - SWC_i)^{10/3}}{\phi^2} \quad (2)$$

285 In Equation 2,  $SWC$  is the soil water content at depth  $i$  (National Ecological Observatory  
286 Network (NEON), 2024e) and  $\phi$  is the porosity(~~Equation 3~~), which in turn is a function of soil  
287 physical properties (National Ecological Observatory Network (NEON), 2024c):

$$\phi = \left(1 - \frac{\rho_s}{\rho_m}\right) (1 - f_V) \quad (3)$$

288 In Equation 3,  $\rho_m$  is the particle density of mineral soil ( $2.65 \text{ g cm}^{-3}$ ),  $\rho_s$  the soil bulk density  
289 ( $\text{g cm}^{-3}$ ) excluding coarse fragments greater than 2 mm (National Ecological Observatory  
290 Network (NEON), 2024c).~~The term~~, and  $f_V$  is a site-specific value that accounts for the  
291 proportion of soil fragments between 2-20 mm. Soil fragments greater than 20 mm were not  
292 estimated due to limitations in the amount of soil that can be analyzed (National Ecological  
293 Observatory Network (NEON), 2024c). We assume ~~there are no pores within rocks~~that rock  
294 fragments contain no internal pores.

295 The ~~second approach to calculate~~ Millington-Quirk model assumes  $\xi$  is ~~the~~ modulated by the  
296 amount of fluid saturation in soil pores (Millington & Shearer, 1971). In contrast, ~~the~~ Marshall  
297 model (Marshall, 1959), ~~where~~ expresses tortuosity as only a function of porosity ( $\xi = \phi^{1.5}$ ),  
298 with  $\phi$  defined from Equation 3. ~~The Marshall model is independent of soil water content and~~  
299 ~~assumes tortuosity is only governed by soil structure. The neonSoilFlux package allows users~~  
300 ~~to choose the tortuosity model most appropriate for site-specific conditions and research goals.~~

301

302 **4.2.3 Soil flux computation**

303 We applied Fick's law (Equation 4) to compute the soil flux  $F_{ij}$  ( $\mu\text{mol m}^{-2} \text{s}^{-1}$ ) across two  
304 soil depths  $i$  and  $j$ :

$$F_{ij} = -D_a \frac{dC}{dz} \quad (4)$$

305 where  $D_a$  is the diffusivity ( $\text{m}^2 \text{s}^{-1}$ ) and  $\frac{dC}{dz}$  is the gradient of CO<sub>2</sub> molar concentration ( $\mu\text{mol}$   
306  $\text{m}^{-3}$ , so the gradient has units of  $\mu\text{mol m}^{-3} \text{m}^{-1}$ ). The soil surface flux is theoretically defined  
307 by applying Equation 4 to measurements collected at the soil surface and directly below the  
308 surface. Measurements of soil temperature, soil water content, and soil CO<sub>2</sub> molar concentration  
309 across the soil profile allow for application of Equation 4 across different soil depths. Each site  
310 had three measurement layers, so we denote the flux ~~between which two layers~~ as a three-digit  
311 subscript  $F_{ijk}$  with indicator variables  $i$ ,  $j$ , and  $k$  indicate if a given layer was used (written in  
312 order of increasing depth), according to the following:

- 313 •  $F_{000}$  is a surface flux estimate using the intercept of the linear regression of  $D_a$  with  
314 depth and the slope from the linear regression of CO<sub>2</sub> with depth (which represents  $\frac{dC}{dz}$   
315 in Fick's Law). Tang et al. (2003) used this approach to compute fluxes in an oak-grass  
316 savannah.
- 317 •  $F_{110}, F_{011}$  are fluxes across the two most shallow layers and two deepest layers respectively.  
318 The diffusivity used in Fick's Law is always at the deeper measurement layer. When used  
319 as a surface flux estimate we assume CO<sub>2</sub> remains constant above this flux depth.
- 320 •  $F_{101}$  is a surface flux estimate using linear extrapolation using concentration measurements  
321 between the shallowest and deepest measurement layer. Hirano et al. (2003) and Tang et  
322 al. (2005) used an approach similar to  $F_{101}$  in a temperate deciduous broadleaf forest  
323 and ponderosa pine forest respectively.

324 Uncertainty in all  $F_{ijk}$  is computed through quadrature (Taylor, 2022).

### 325 4.3 Post processing evaluation

326 Following collection of field measurements and calculation of the soil fluxes from `neonSoilFlux`  
327 package, we compared measured  $F_S$  based on closed-dynamic chamber measurements with  
328 the LI-COR instruments to a given soil flux calculation from `neonSoilFlux` for each site and  
329 flux computation method. Statistics included the ~~associated R<sup>2</sup> value~~, ~~slope from a linear~~  
330 ~~regression (m)~~, ~~normalized~~ root mean squared error (~~RMSE~~<sup>NRMSE</sup>), and ~~signal to noise ratio~~  
331 ~~(SNR)~~, ~~defined as the ratio of a modeled soil flux ( $F_{ijk}$ ) from neonSoilFlux to its quadrature~~  
332 ~~uncertainty ( $\sigma_{ijk}$ ) associated R<sup>2</sup> value~~.

333 We observed that the range of values (e.g.  $F_{ijk} \pm \sigma_{ijk}$  was much larger than the measured field  
334 flux. We evaluated  $|F_S - F_{ijk}| \ll (1 - \epsilon)\sigma_{ijk}$ , where  $F_S$  is a measured field soil flux from the  
335 LI-COR 6800 (as the LI-COR 870/8250 was used at only three sites in 2024 but the 6800  
336 was used at all sites in both years). The parameter  $\epsilon$  was an uncertainty reduction factor to  
337 evaluate how much the quadrature uncertainty could be reduced while maintaining precision  
338 between modeled  $F_{ijk}$  and measured  $F_S$ .

339 Finally, for a half-hourly interval we also computed a *post hoc*  $D_a$  using the LI-COR flux along  
340 with the CO<sub>2</sub> surface gradient reported by NEON using the measurement levels closest to the  
341 surface.

## 342 5 Results

343 Our overall goal was to design and validate an R package to estimate soil carbon dioxide  
344 fluxes fluxes across terrestrial NEON sites using the flux gradient method. Validation of the

345 approach was based on comparison of estimated fluxes to field measurements made at six  
346 focal sites. We first present our field measurement results, then the concordance between the  
347 modeled and measured results, and lastly assess the factors that influenced the success of the  
348 modeled approach at a given site.

349 **5.1 Concordance between modelled and measured soil CO<sub>2</sub> flux**

350 **5.2 Field measurements**

351 We visited six NEON sites in the summers of 2022 and 2024. Using a closed dynamic chamber  
352 approach, we quantified soil carbon dioxide fluxes over the course of a week at each site. The  
353 sites we visited ranged substantially in both their annual average temperature and precipitation  
354 as well as their biome type (Table 2). These differences also influenced the wide range of observed  
355 flux rates across sites. We used a LI-6800 to take manual hourly measurements at the sites we  
356 visited in 2022 (SRER, SJER, WREF) and half-hourly manual measurements for the sites we  
357 visited in 2024 (UNDE, KONZ, WOOD). In 2024 we also used an automated chamber system  
358 (LI-870/LI-8250) to take half-hourly measurements 24 hours a day, thereby also capturing  
359 nighttime fluxes in addition to the daytime fluxes also measured with the LI-6800.

360 **5.2**

361 The timeseries of the measured fluxes from the LI-COR 6800 and 870/8250 were compared  
362 to modeled soil fluxes from the `neonSoilFlux` R package (Figure 4). We also assessed year-  
363 long estimated flux time series and compared those to field measurements made at each site  
364 (Figure 5). Results are reported in local time. Where applicable, sites are displayed from left  
365 to right by increasing soil temperature (Table 1). Positive values of the flux indicate that there  
366 is a flux moving towards the surface. Overall, with the exception of SRER (discussed later) the

Table 2: Summary of measured soil characteristics and flux results from field measurements across six NEON sites using a LI-COR 6800 (LI-870/8250 measurements omitted to enable direct comparability) via the closed-dynamic chamber method. Numeric values for soil CO<sub>2</sub> flux, soil temperature, and volumetric soil water content (VSWC) are the mean and standard deviation of field measurements at each site.

| Site | Flux<br>μmol m <sup>-2</sup> s <sup>-1</sup> | Soil temp<br>°C | VSWC<br>cm <sup>3</sup> cm <sup>-3</sup> | n  |
|------|----------------------------------------------|-----------------|------------------------------------------|----|
| UNDE | 2.55 ± 0.26                                  | 14.33 ± 0.77    | 0.33 ± 0.02                              | 61 |
| WOOD | 3.02 ± 0.4                                   | 16.01 ± 1.54    | 0.28 ± 0.01                              | 53 |
| WREF | 3.62 ± 0.3                                   | 15.34 ± 1.76    | 0.27 ± 0.06                              | 21 |
| KONZ | 6.35 ± 0.97                                  | 27.28 ± 4.14    | 0.37 ± 0.01                              | 44 |
| SJER | 0.94 ± 0.02                                  | 41.68 ± 11.22   | 0.01 ± 0.01                              | 32 |
| SRER | 0.72 ± 0.09                                  | 47.64 ± 7.46    | 0.04 ± 0.01                              | 32 |

367 computed fluxes determined using a variety of plausible methods spanned the field-measured  
 368 fluxes, but the specific flux-gradient method that best approximated field measurements varied  
 369 by site.

## 370 5.2 Assessment of data gaps

371 For a given half-hourly time period, the We calculated the statistical 1-1 comparison between  
 372 the various estimates of soil flux computed by neonSoilFlux packages assigns a QA flag  
 373 for a measurement if more one values across all measurement depths uses gap-filled data  
 374 (Section 4.2.1). Panel a of Figure ?? reports the proportion of gap-filled data for all input  
 375 environmental measurements at each site during the period when field measurements were  
 376 made. Soil fluxes are computed from 4 different types of input measurements ( $T_S$ ,  $SWC$ ,  
 377  $P$ , and  $CO_2$ ), any of which could have a QA flag in a with the field-measured fluxes within  
 378 half-hourly interval. Panel b of Figure ?? displays at each site the distribution of the number  
 379 of different gap-filled measurements used to compute a half-hourly flux. The largest cause of  
 380 measurements needing to be gap-filled was missing or flagged soil moisture data. Calculating

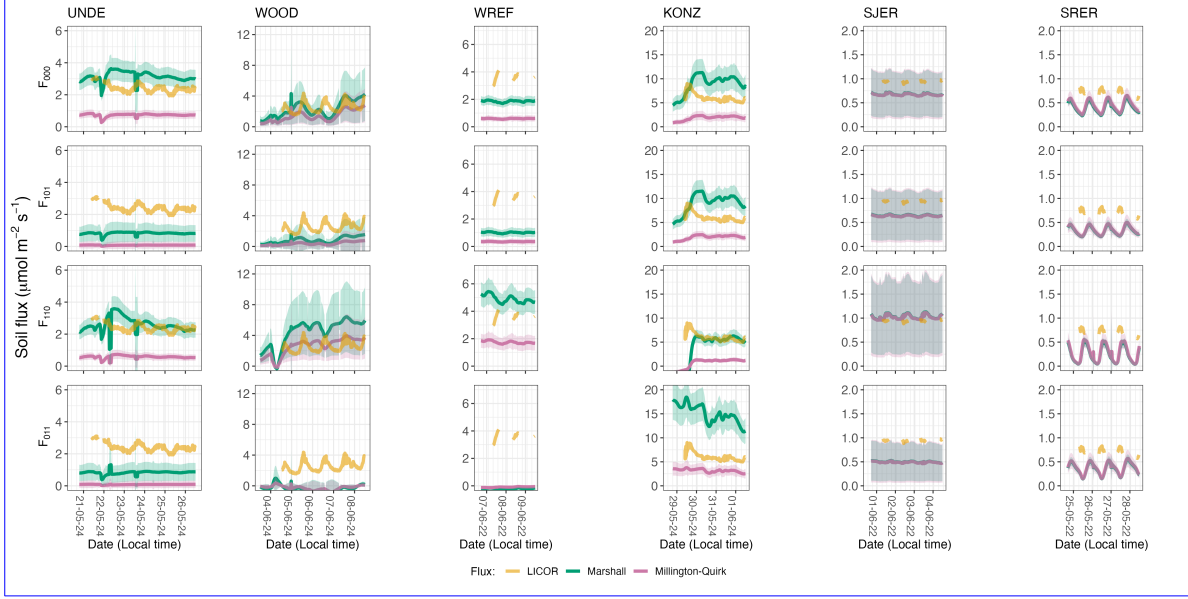


Figure 4: Timeseries of ~~both measured~~ soil surface flux ( $F_s$ ) from LICOR measured (yellow ~~circles~~  
~~lines~~) and modeled soil fluxes (green or purple lines) by the `neonSoilFlux` R package. Fluxes from the `neonSoilFlux` R package are separated by the diffusivity model used (Millington-Quirk or Marshall, Section 4.2.2). ~~Vertical~~ Individual vertical axis labels in the first column represent the measurement levels where the flux-gradient approach is applied (Section 4.2.3). Ribbons for modeled soil fluxes represent  $\pm 1$  standard deviation. Results are reported in local time.

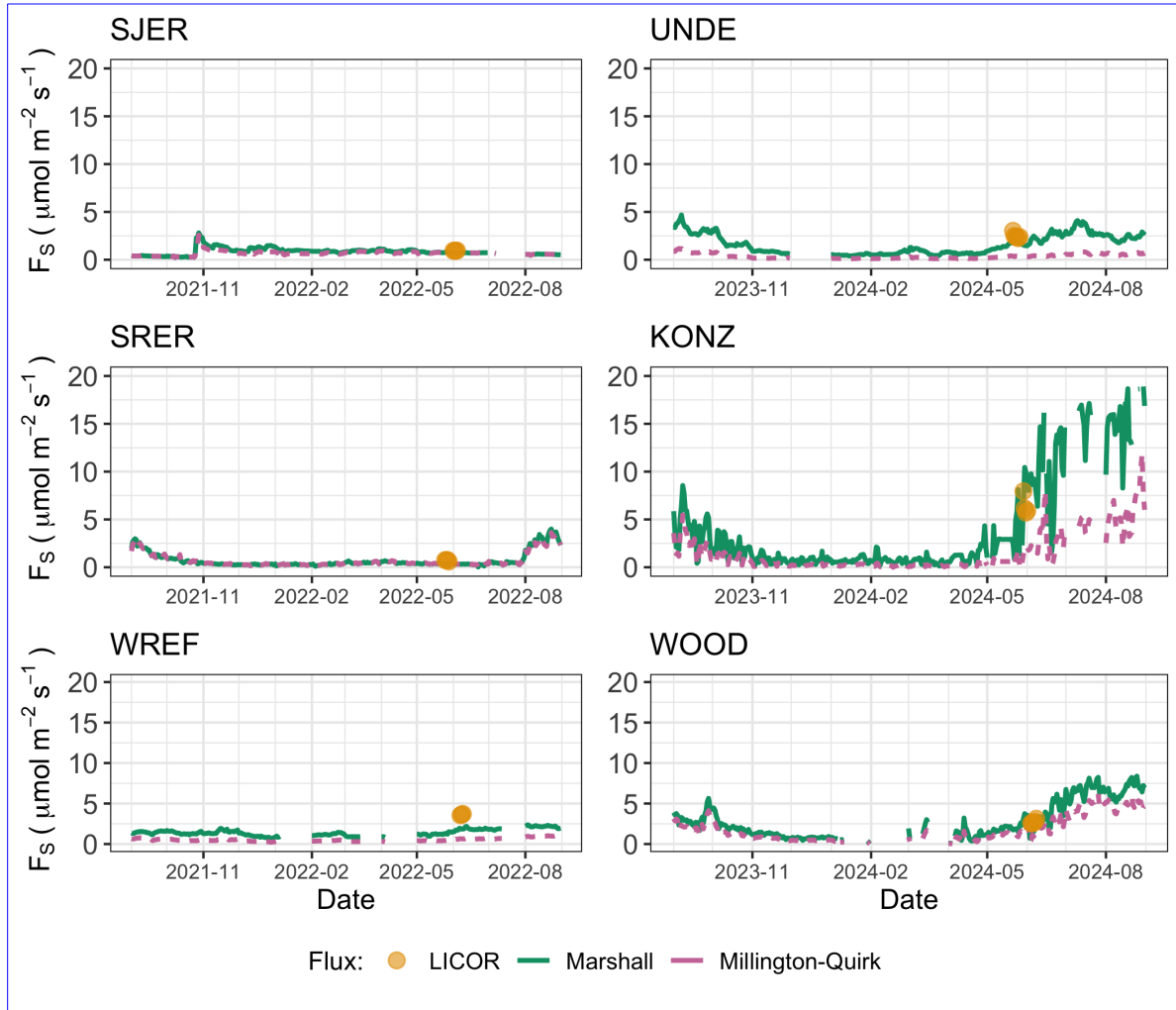


Figure 5: Timeseries of both daily-averaged field  $F_S$  (yellow circles) and daily ensemble averaged soil fluxes (average of  $F_{000}$ ,  $F_{101}$ ,  $F_{011}$ ,  $F_{110}$ , Section 4.2.3) by the `neonSoilFlux` R package, separated by the diffusivity model used (green or purple lines, Millington-Quirk or Marshall, Section 4.2.2).

381 fluxes for WOOD and SJER required using the largest proportion of gap-filled measurements,  
382 due to substantially large fractions of flagged or missing SWC and  $T_S$  data. periods. Statistics  
383 for these comparisons are reported in Table 3.

384 **5.2 Assessing the signal to noise ratio (SNR) and evaluating estimated  
385 uncertainties**

386 The computed signal to noise ratio (SNR) and the proportion of measured field fluxes within  
387 the modeled uncertainty for a given flux computation method  $F_{ijk}$  suggest that there was  
388 substantial variability in the agreement between the gradient method and field-measured  
389 observations (Figure ??, Section 4.3). Here, values of SNR greater than unity indicate lower  
390 reported uncertainty, as propagated by quadrature due to a relatively higher precision of  
391 measured input variables ( $\text{CO}_2$ ,  $T_S$ , SWC, or  $P$ ).

392 The sensitivity to an uncertainty reduction factor ( $\epsilon$ , bottom panels in Figure ??) demonstrates  
393 how concordance between measured and modeled fluxes would be affected if environmental  
394 measurement uncertainty  $\sigma_{ijk}$  were to decrease. As  $\epsilon$  increases from left to right in each figure,  
395 the possible range of values for each predicted flux value decreases and the proportion of  
396 measured fluxes that fall within that range also decreases.

397 Top panels: distribution of SNR values across each of the different sites for modeled  
398 effluxes from the `neonSoilFlux` package, depending on the diffusivity calculation used  
399 (Millington-Quirk or Marshall, Section 4.2.2). Bottom panels: Proportion of measured  $F_S$   
400 within the modeled range of a flux computation method  $F_{ijk}$  given an uncertainty reduction  
401 factor  $\epsilon$ , or  $|F_S - F_{ijk}| < (1 - \epsilon)\sigma_{ijk}$ .

Table 3: Statistical comparison between measured fluxes at each site with fluxes reported by `neonSoilFlux` with the different diffusivity calculations applied.  $m$  refers to the slope of a linear regression between the LICOR measured fluxes at each site and the outputs from `neonSoilFlux`. \* = significance at the 5% level, \*\* = significance at the 1% level. NRMSE is the normalized root mean square error between measured and `neonSoilFlux` outputs, normalized by the sample mean of the LICOR measured fluxes.

**Panel a)** Proportion of input gap-filled environmental measurements used to generate  $F_S$  from the `neonSoilFlux` package, by study site. **Panel b)** distribution of the usage of gap-filled measurements at each site.

|             | Millington-Quirk |       |       | Marshall |       |       |
|-------------|------------------|-------|-------|----------|-------|-------|
|             | $m$              | NRMSE | $R^2$ | $m$      | NRMSE | $R^2$ |
| <b>KONZ</b> |                  |       |       |          |       |       |
| $F_{110}$   | -0.39**          | 0.87  | 0.41  | -1.86**  | 0.63  | 0.41  |
| $F_{101}$   | -0.12**          | 0.69  | 0.22  | -0.44**  | 0.60  | 0.15  |
| $F_{011}$   | 0.16**           | 0.52  | 0.20  | 1**      | 1.35  | 0.25  |
| $F_{000}$   | -0.12**          | 0.70  | 0.23  | -0.41**  | 0.58  | 0.14  |
| <b>SJER</b> |                  |       |       |          |       |       |
| $F_{110}$   | -0.7*            | 0.13  | 0.17  | -0.76*   | 0.14  | 0.18  |
| $F_{101}$   | -0.23*           | 0.32  | 0.21  | -0.25**  | 0.31  | 0.24  |
| $F_{011}$   | -0.07            | 0.49  | 0.02  | -0.09    | 0.48  | 0.03  |
| $F_{000}$   | -0.33*           | 0.29  | 0.17  | -0.37*   | 0.28  | 0.18  |
| <b>SRER</b> |                  |       |       |          |       |       |
| $F_{110}$   | -0.06            | 0.56  | 0.00  | -0.05    | 0.59  | 0.00  |
| $F_{101}$   | -0.34**          | 0.66  | 0.53  | -0.33**  | 0.67  | 0.52  |
| $F_{011}$   | -0.44**          | 0.69  | 0.49  | -0.42**  | 0.70  | 0.49  |
| $F_{000}$   | -0.48**          | 0.58  | 0.51  | -0.44**  | 0.61  | 0.51  |
| <b>UNDE</b> |                  |       |       |          |       |       |
| $F_{110}$   | -0.09**          | 0.77  | 0.06  | -0.29*   | 0.25  | 0.02  |
| $F_{101}$   | -0.01**          | 0.97  | 0.10  | -0.1**   | 0.66  | 0.14  |
| $F_{011}$   | -0.01**          | 0.97  | 0.05  | -0.09**  | 0.66  | 0.04  |
| $F_{000}$   | -0.11**          | 0.70  | 0.16  | -0.29**  | 0.36  | 0.06  |
| <b>WOOD</b> |                  |       |       |          |       |       |
| $F_{110}$   | 0.27**           | 0.31  | 0.10  | 0.32**   | 0.97  | 0.06  |
| $F_{101}$   | 0.11**           | 0.87  | 0.16  | 0.19**   | 0.69  | 0.13  |
| $F_{011}$   | 0.1**            | 1.12  | 0.10  | 0.23**   | 1.24  | 0.11  |
| $F_{000}$   | 0.39**           | 0.47  | 26    | 0.55**   | 0.36  | 0.15  |
| <b>WREF</b> |                  |       |       |          |       |       |
| $F_{110}$   | -0.17**          | 0.53  | 0.78  | -0.52**  | 0.35  | 0.75  |
| $F_{101}$   | -0.02*           | 0.91  | 0.24  | -0.05**  | 0.73  | 0.35  |
| $F_{011}$   | 0.05**           | 1.03  | 0.37  | 0.16**   | 1.07  | 0.37  |
| $F_{000}$   | 0                | 0.84  | 0.00  | -0.03    | 0.49  | 0.05  |

402 **5.2 Effects of method choice on diffusivity estimates**

403 We assessed the distribution of  $D_a$  (from both the Marshall and Millington-Quirk methods)  
404 at each study site, and also computed a *post hoc* estimate of  $D_a$  using field surface flux  
405 measurements (Section 4.2.2). For the field-estimated measurements we omitted negative  
406 values of  $D_a$ , as that indicates the CO<sub>2</sub> gradient decreases with soil depth (thereby violating  
407 assumptions of the flux-gradient method, which is our focus here). In four of six field sites, the  
408 *post hoc*  $D_a$  estimate fell roughly between the two diffusion estimation methods; however this  
409 was less the case in the two driest sites, SJER and SRER (Table 1), where the field estimate of  
410 diffusivity was either lower or higher than both of the other methods (Figure 6).

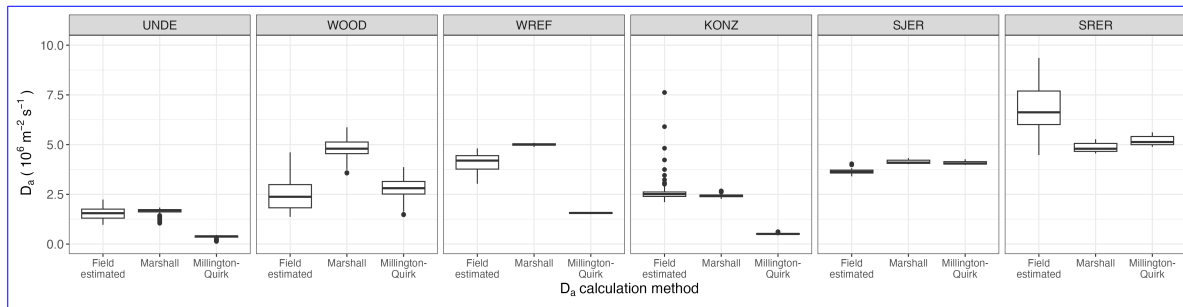


Figure 6: Distribution of diffusivity ( $D_a$ ) at each study site. Values of  $D_a$  were provided by the `neonSoilFlux` package, computed from the Millington-Quirk or Marshall models (Section 4.2.2). A post-hoc estimate of diffusivity (labeled as “Field estimated”) was computed through the field measured flux (Figure 4), divided by the CO<sub>2</sub> gradient from the measurement levels closest to the soil surface, as reported by NEON. We only used  $F_S$  measured by the LICOR 6800 at all sites to standardize comparisons.

411 **6 Discussion**

412 This study presents a unified data science workflow to efficiently process automated measure-  
413 ments of belowground soil CO<sub>2</sub> concentrations, soil water content, and soil temperature to  
414 infer estimates of soil surface CO<sub>2</sub> effluxes through application of Fick’s Law (Equation 4).

415 Our core goals in this study were: (1) to generate estimates of soil flux from continuous soil  
416 sensor data at terrestrial NEON sites using the flux-gradient method and then (2) to compare  
417 those estimates to field-measured fluxes based on the closed chamber approach at six NEON  
418 focal sites. We discuss our progress toward these core goals through (1) an overall evaluation  
419 of the flux-gradient approach (and uncertainty calculation) and (2) site-specific evaluation of  
420 differences in estimated vs measured fluxes.

## 421 **6.1 General evaluation of flux-gradient approach**

422 Key assumptions of the flux-gradient approach are that CO<sub>2</sub> concentrations increase through-  
423 out the soil profile such that the highest concentrations are observed in the deepest lay-  
424 ers. Additionally, field flux measurements should correlate with  $F_{000}$  because they represent  
425 surface fluxes. Periods where this gradient condition are not met generally are connected  
426 to processes that occur during soil wetting events, where more shallow soil layers produce  
427 higher concentrations of CO<sub>2</sub> due to microbial respiration pulses following rewetting. This  
428 effect is likely to be largest at sites with rich organic soils (e.g. KONZ). Based on this  
429 reasoning, in these types of situations we would *a priori* expect  $F_{011} \leq F_{101} \leq F_{110} \leq F_{000}$   
430  $F_{011}$  (deepest layers)  $\leq F_{101} \leq F_{110}$  (shallow layers)  $\leq F_{000}$  (all layers) because the previous  
431 flux estimates rely primarily on CO<sub>2</sub> concentrations at deeper depths, and could miss high  
432 concentrations of CO<sub>2</sub> produced in shallower layers.

433 When modeling soil respiration, typically a non-linear response function that also considers  
434 soil type is used (Bouma & Bryla, 2000; Yan et al., 2016, 2018). For the `neonSoilFlux`  
435 package, soil type is connected to the measurement of bulk density, which was characterized  
436 at each NEON site. This bulk density estimate is based on replicate samples collected from  
437 the site megapit at a subset of soil horizons, with an estimated uncertainty of ±5% (National  
438 Ecological Observatory Network (NEON), 2024c). Coarse fragment estimates also have very

<sup>439</sup> large uncertainties, but because the volume fraction tends to be low in surface soils it probably  
<sup>440</sup> wouldn't contribute much additional flux uncertainty.

<sup>441</sup> Our results suggest that the most important way to improve reliability of the flux estimate is  
<sup>442</sup> to reduce the usage of gap-filled data. The current approach to gap filling in `neonSoilFlux`  
<sup>443</sup> uses monthly mean data to gap fill—this approach decreases the ability of the estimate to  
<sup>444</sup> be responsive to ~~short turn~~short-term pulses that occur with rapid weather shifts. Four sites  
<sup>445</sup> (KONZ, SRER, WREF, and UNDE) had more than 75% of half-hourly periods with no-gap  
<sup>446</sup> filled measurements ([Figure S1, Supplementary Information](#)). Two sites (SJER and WOOD)  
<sup>447</sup> had more than 75% of half-hourly intervals with just one gap-filled measurement. While we did  
<sup>448</sup> not need to use gap-filled measurements to compute the flux at WREF, field data collection  
<sup>449</sup> occurred following a severe rainstorm, with soils at the beginning of the sampling week near  
<sup>450</sup> their water holding capacity. We recommend that whenever possible, knowledge of local field  
<sup>451</sup> conditions should influence analysis decisions in addition to any QA filtering protocols in the  
<sup>452</sup> `neonSoilFlux` package.

<sup>453</sup> We recognize that this gap-filling approach may lead to gap-filled values that are quite different  
<sup>454</sup> from the actual values, such as an underestimate of soil moisture following rain events. Further  
<sup>455</sup> extensions of the gap filling method could use more sophisticated gap-filling routines, similar to  
<sup>456</sup> what is used for net ecosystem carbon exchange (Falge et al., 2001; Liu et al., 2023; Mariethoz  
<sup>457</sup> et al., 2015; Moffat et al., 2007; Zhang et al., 2023). The current gap-filling routine provides a  
<sup>458</sup> consistent approach that can be applied to each data stream, but further work may explore  
<sup>459</sup> alternative gap-filling approaches.

**460 6.2 Evaluation of flux-gradient approach at each site**

461 Derived results from the `neonSoilFlux` package have patterns that are broadly consistent with  
462 those directly measured in the field (Figure 4 and Figure 5), even though statistical comparisons  
463 between the field-measured and `neonSoilFlux` values were quite variable and poor (e.g.  $R^2$   
464 ranging from 0.00 to 0.78; Table 3). One advantage of the `neonSoilFlux` package is its ability  
465 to calculate fluxes across different soil depths (Figure 3), which allows for additional site-specific  
466 customization. We believe the package can provide a useful baseline estimate of soil fluxes that  
467 can always be complemented through additional field measurements.

468 The six locations studied provide a range of case studies that suggest different considerations  
469 may apply to different sites when applying the flux-gradient method. For example, the Santa  
470 Rita Experimental Range (SRER) is a desert site characterized by sandy soil, which also was  
471 the location of the highest field soil temperatures that we observed (Table 2). At SRER the  
472 flux across the top two layers ( $F_{110}$ ) produced a pattern of soil flux most consistent with the  
473 observed field data. The remaining methods  $F_{101}$ ,  $F_{011}$ , or  $F_{000}$  are derived from information  
474 taken from the deepest layer, which seems to have been decoupled from the surface layers both  
475 in terms of temperature and CO<sub>2</sub> concentration. This may be a general circumstance where  
476 there are large diurnal temperature extremes that rapidly change during the course of a day  
477 and overnight, leading to lags in the timing of when temperature increases propagate down to  
478 deeper soil layers.

479 Immediately prior to our visit to Konza Prairie (KONZ), that site that experienced a significant  
480 rain event that led to wet soils that gradually dried out over the course of our time there.  
481 This pulse of precipitation increased the soil CO<sub>2</sub> concentration at the top layer above the  
482 concentrations in lower layers, leading to negative estimated flux values at the start of the  
483 experiment. In this case it was only when the soil began to return to a baseline level that the  
484 assumptions of the flux-gradient method were again met.

485 Thus, when Both of the previous cases also provide context for the poor statistical comparisons  
486 between field-measured soil fluxes and `neonSoilFlux` outputs Table 3. When considering sys-  
487 tematic deployment of this method across a measurement network, there are a number of  
488 independent challenges that require careful consideration. There are clear tradeoffs between  
489 (1) accuracy of modeled fluxes (defined here as closeness to field-measured  $F_S$  and the uncer-  
490 tainty reduction factor  $\epsilon$ ), (2) precision (which could be defined by the SNR~~signal to noise~~  
491 ~~ratio~~), and (3) the choice of the diffusivity model (Section 4.2.2) or flux computation method  
492 (Section 4.2.3)~~used (Figure ??).~~ There was no predictable pattern in SNR for either the flux  
493 computation method or diffusivity calculation, indicating that output uncertainty is driven  
494 primarily by input. A sensitivity analysis (Figure S2, Supplemental Information) found that  
495 flux output uncertainty was dominated by measurement uncertainty ( $T_S$ ,  $P$ , SWC, or CO<sub>2</sub>)  
496 .—Across the different fluxcomputation methods, the proportion of measured fluxes where  
497  $|F_S - F_{ijk}| < (1 - \epsilon)\sigma_{ijk}$  decreased as  $\epsilon$  increased, except where field  $F_S$  was already outside  
498 of the modeled range (i.e. UNDE and WREF). The method rather than the diffusivity method  
499 to compute soil flux. Notably, the  $F_{110}$  (where soil flux was computed from the top two soil  
500 layers) was the least sensitive to the uncertainty reduction factor ( $\epsilon$ ). This lack of sensitivity  
501 could represent that a surface chamber-based measurement method (e.g. with a LI-COR  
502 instrument) measures the flux up out of the surface layer and thus is most closely related  
503 to assumptionsand measurements inherent in the  $F_{110}$  methodmethod was least sensitivty  
504 to measurement uncertainty likely because it best aligns with surface chamber measurement  
505 assumptions.

506 Finally, comparing the effects of different diffusivity estimation methods on the match between  
507 modeled and measured fluxes (Figure 5) highlights the sensitivity of  $F_{ijk}$  to diffusivity. The  
508 comparison between diffusivity estimates compared to field estimated diffusivity (Figure 6)  
509 demonstrates that site parameters can dictate which measure of diffusivity is most likely to  
510 be accurate in a given environmental context. Site-specific differences a largely a reflection of

511 differences in soil moisture across the sites (Table 1), as not all diffusivity estimation methods  
512 incorporate soil moisture equivalently. While we here have compares two approaches to calculate  
513 diffusivity (the Millington-Quirk and Marshall models), it may be valuable to evaluate other  
514 diffusivity models (e.g. the Moldrup model; Moldrup et al. (1999)) as well. Ultimately the  
515 choice of a particular diffusivity model could be determined based on knowledge of site-specific  
516 evaluations or a set of these models could be used to generate a model ensemble average as a  
517 means to trade precision for a more general approach.

### 518 **6.3 Recommendations for future method development**

519 The `neonSoilFlux` package provides ~~three different~~ several approaches to estimate soil flux  
520 using the gradient method. We believe these approaches enable the software to be used across  
521 a range of site-specific assumptions (Maier & Schack-Kirchner, 2014). We note, however, that  
522 this choice can have a determinative approach on the calculated values. Ensemble averaging  
523 approaches (Elshall et al., 2018; Raftery et al., 2005) may be one way to address this problem  
524 if the goal is to calculate fluxes using the same method at a diverse range of different sites.  
525 Two other ideas would be to apply machine learning algorithms (e.g. random ~~trees~~forests)  
526 to generate a single flux estimate across diverse sites, or using co-located estimates of net  
527 ecosystem carbon exchange from eddy-flux towers to further constrain results or to assess soil  
528 flux results for plausibility ~~–(Phillips et al., 2017)~~.  
529 These challenges notwithstanding, the method used here and made available in the  
530 `neonSoilFlux` R package has the potential to produce nearly continuous estimates of flux  
531 across all terrestrial NEON sites. These estimates are a significant improvement on available  
532 approaches to constrain the portion of ecosystem respiration attributable to the soil. This, in  
533 turn, also aids in our ability to understand the soil contribution to the net ecosystem flux  
534 measured at these sites using the co-located eddy flux towers.

## 535 7 Conclusions

536 We have here presented an used the R package `neonSoilFlux` for the estimation of soil CO<sub>2</sub>  
537 fluxes to test its broader application in estimating soil CO<sub>2</sub> fluxes with the flux-gradient  
538 method, using data from continuous buried soil sensor measurements across terrestrial National  
539 Ecological Observatory Network sensors at NEON terrestrial sites. We compared the predicted  
540 fluxes to those measured directly using a field-based closed chamber approach. We find  
541 that the flux gradient method, while Soil fluxes from `neonSoilFlux` were broadly effective  
542 at producing estimates of flux comparable to those measured in the field using a chamber-  
543 based technique, is. However `neonSoilFlux` outputs are quite sensitive to a number of  
544 issues, including most prominently: missing data (and thus gap-filling of input measurement  
545 datasets), the selection of soil depths used to best calculate the gradient (which may vary  
546 between sites), and finally the choice of method used for estimating soil diffusivity. Despite  
547 these challenges, the broad geographic scale and high temporal resolution of the NEON data  
548 make a compelling case for continued efforts to refine this approach to help us understand how  
549 The flexibility of the `neonSoilFlux` package allows the user to evaluate each of these issues  
550 with site-specific knowledge and contexts. Future refinements and subsequent validation of  
551 `neonSoilFlux` outputs will feed forward into evaluating soil carbon fluxes broader spatial  
552 scales to enhance understanding of the ways in which soils across diverse ecosystems are  
553 responding to a changing climate.

## 554 Sources Cited

555 Ayres, E., Reichle, R. H., Colliander, A., Cosh, M. H., & Smith, L. (2024). Validation of  
556 Remotely Sensed and Modeled Soil Moisture at Forested and Unforested NEON Sites.

- 557      *IEEE Journal of Selected Topics in Applied Earth Observations and Remote Sensing*, 17,  
558      14248–14264. <https://doi.org/10.1109/JSTARS.2024.3430928>
- 559      Baldocchi, D. (2014). Measuring fluxes of trace gases and energy between ecosystems and the  
560      atmosphere - the state and future of the eddy covariance method. *Global Change Biology*,  
561      20(12), 3600–3609. <https://doi.org/10.1111/gcb.12649>
- 562      Berenbaum, M. R., Carpenter, S. R., Hampton, S. E., Running, S. W., & Stanzione, D. C.  
563      (2015). *Report from the NSF BIO Advisory Committee Subcommittee on NEON Scope  
564      Impacts*.
- 565      Bond-Lamberty, B. (2018). New Techniques and Data for Understanding the Global Soil  
566      Respiration Flux. *Earth's Future*, 6(9), 1176–1180. <https://doi.org/10.1029/2018EF000866>
- 567      Bond-Lamberty, B., Ballantyne, A., Berryman, E., Fluet-Chouinard, E., Jian, J., Morris, K.  
568      A., Rey, A., & Vargas, R. (2024). Twenty Years of Progress, Challenges, and Opportuni-  
569      ties in Measuring and Understanding Soil Respiration. *Journal of Geophysical Research:  
570      Biogeosciences*, 129(2), e2023JG007637. <https://doi.org/10.1029/2023JG007637>
- 571      Bond-Lamberty, B., Christianson, D. S., Malhotra, A., Pennington, S. C., Sihi, D., AghaK-  
572      ouchak, A., Anjileli, H., Altaf Arain, M., Armesto, J. J., Ashraf, S., Ataka, M., Baldocchi,  
573      D., Andrew Black, T., Buchmann, N., Carbone, M. S., Chang, S.-C., Crill, P., Curtis, P.  
574      S., Davidson, E. A., ... Zou, J. (2020). COSORE: A community database for continuous  
575      soil respiration and other soil-atmosphere greenhouse gas flux data. *Global Change Biology*,  
576      26(12), 7268–7283. <https://doi.org/10.1111/gcb.15353>
- 577      Bond-Lamberty, B., & Thomson, A. (2010). A global database of soil respiration data.  
578      *Biogeosciences*, 7(6), 1915–1926. <https://doi.org/10.5194/bg-7-1915-2010>
- 579      Bond-Lamberty, B., Wang, C., & Gower, S. T. (2004). A global relationship between the  
580      heterotrophic and autotrophic components of soil respiration? *Global Change Biology*,  
581      10(10), 1756–1766. <https://doi.org/10.1111/j.1365-2486.2004.00816.x>
- 582      Bouma, T. J., & Bryla, D. R. (2000). On the assessment of root and soil respiration for soils of

- 583 different textures: Interactions with soil moisture contents and soil CO<sub>2</sub> concentrations.
- 584 *Plant and Soil*, 227(1), 215–221. <https://doi.org/10.1023/A:1026502414977>
- 585 Chen, H., & Tian, H.-Q. (2005). Does a General Temperature-Dependent Q10 Model of Soil  
586 Respiration Exist at Biome and Global Scale? *Journal of Integrative Plant Biology*, 47(11),  
587 1288–1302. <https://doi.org/10.1111/j.1744-7909.2005.00211.x>
- 588 Davidson, E. A., Janssens, I. A., & Luo, Y. (2006). On the variability of respiration in  
589 terrestrial ecosystems: Moving beyond Q10. *Global Change Biology*, 12, 154–164. <https://doi.org/10.1111/j.1365-2486.2005.01065.x>
- 590 Desai, A. R., Murphy, B. A., Wiesner, S., Thom, J., Butterworth, B. J., Koupaei-Abyazani, N.,  
591 Muttaqin, A., Paleri, S., Talib, A., Turner, J., Mineau, J., Merrelli, A., Stoy, P., & Davis,  
592 K. (2022). Drivers of Decadal Carbon Fluxes Across Temperate Ecosystems. *Journal of  
593 Geophysical Research: Biogeosciences*, 127(12), e2022JG007014. <https://doi.org/10.1029/2022JG007014>
- 594 595
- 596 Efron, B., & Tibshirani, R. J. (1994). *An Introduction to the Bootstrap*. Chapman and  
597 Hall/CRC. <https://doi.org/10.1201/9780429246593>
- 598 Elshall, A. S., Ye, M., Pei, Y., Zhang, F., Niu, G.-Y., & Barron-Gafford, G. A. (2018). Relative  
599 model score: A scoring rule for evaluating ensemble simulations with application to microbial  
600 soil respiration modeling. *Stochastic Environmental Research and Risk Assessment*, 32(10),  
601 2809–2819. <https://doi.org/10.1007/s00477-018-1592-3>
- 602 Falge, E., Baldocchi, D., Olson, R., Anthoni, P., Aubinet, M., Bernhofer, C., Burba, G.,  
603 Ceulemans, R., Clement, R., Dolman, H., Granier, A., Gross, P., Grünwald, T., Hollinger,  
604 D., Jensen, N.-O., Katul, G., Keronen, P., Kowalski, A., Lai, C. T., ... Wofsy, S. (2001).  
605 Gap filling strategies for defensible annual sums of net ecosystem exchange. *Agricultural  
606 and Forest Meteorology*, 107(1), 43–69. [https://doi.org/10.1016/S0168-1923\(00\)00225-2](https://doi.org/10.1016/S0168-1923(00)00225-2)
- 607 Farrance, I., & Frenkel, R. (2012). *Uncertainty of Measurement: A Review of the Rules  
608 for Calculating Uncertainty Components through Functional Relationships*. *The Clinical*

- 609 *Biochemist Reviews*, 33(2), 49–75.
- 610
- 611 Friedlingstein, P., O’Sullivan, M., Jones, M. W., Andrew, R. M., **Bakker, D. C. E.**, Hauck, J.,  
612 Landschützer, P., Le Quéré, C., Li, H., Luijkh, I. T., Olsen, A., Peters, G. P., Peters, W.,  
613 Pongratz, J., Schwingshakl, C., Sitch, S., Canadell, J. G., Ciais, P., Jackson, R. B., Alin, S.  
614 R., **Anthoni, P.**, ... **Zheng, B.** (2023) ... **Zeng, J.** (2025). Global Carbon Budget 2023–2024.  
615 *Earth System Science Data*, 5301–5369–17(3), 965–1039. <https://doi.org/10.5194/essd-17-965-2025>
- 616
- 617 Hamdi, S., Moyano, F., Sall, S., Bernoux, M., & Chevallier, T. (2013). Synthesis analysis  
618 of the temperature sensitivity of soil respiration from laboratory studies in relation to  
619 incubation methods and soil conditions. *Soil Biology and Biochemistry*, 58, 115–126.  
620 <https://doi.org/10.1016/j.soilbio.2012.11.012>
- 621
- 622 Hirano, T., Kim, H., & Tanaka, Y. (2003). Long-term half-hourly measurement of soil CO<sub>2</sub>  
623 concentration and soil respiration in a temperate deciduous forest. *Journal of Geophysical  
624 Research: Atmospheres*, 108(D20). <https://doi.org/10.1029/2003JD003766>
- 625 Jackson, R. B., Lajtha, K., Crow, S. E., Hugelius, G., Kramer, M. G., & Piñeiro, G. (2017).  
626 The Ecology of Soil Carbon: Pools, Vulnerabilities, and Biotic and Abiotic Controls.  
627 *Annual Review of Ecology, Evolution and Systematics*, 48(Volume 48, 2017), 419–445.  
628 <https://doi.org/10.1146/annurev-ecolsys-112414-054234>
- 629 Jian, J., Bailey, V., Dorheim, K., Konings, A. G., Hao, D., Shiklomanov, A. N., Snyder,  
630 A., Steele, M., Teramoto, M., Vargas, R., & Bond-Lamberty, B. (2022). Historically  
631 inconsistent productivity and respiration fluxes in the global terrestrial carbon cycle. *Nature  
632 Communications*, 13(1), 1733. <https://doi.org/10.1038/s41467-022-29391-5>
- 633 Jian, J., Vargas, R., Anderson-Teixeira, K., Stell, E., Herrmann, V., Horn, M., Kholod, N.,  
634 Manzon, J., Marchesi, R., Paredes, D., & Bond-Lamberty, B. (2021). A restructured and

- 635 updated global soil respiration database (SRDB-V5). *Earth System Science Data*, 13(2),  
636 255–267. <https://doi.org/10.5194/essd-13-255-2021>
- 637 Jiang, J., Feng, L., Hu, J., Liu, H., Zhu, C., Chen, B., & Chen, T. (2024). Global soil  
638 respiration predictions with associated uncertainties from different spatio-temporal data  
639 subsets. *Ecological Informatics*, 82, 102777. <https://doi.org/10.1016/j.ecoinf.2024.102777>
- 640 Jobbágy, E. G., & Jackson, R. B. (2000). The Vertical Distribution of Soil Organic Carbon  
641 and its Relation to Climate and Vegetation. *Ecological Applications*, 10(2), 423–436.  
642 [https://doi.org/10.1890/1051-0761\(2000\)010%5B0423:TVDOSO%5D2.0.CO;2](https://doi.org/10.1890/1051-0761(2000)010%5B0423:TVDOSO%5D2.0.CO;2)
- 643 Liu, K., Li, X., Wang, S., & Zhang, H. (2023). A robust gap-filling approach for European  
644 Space Agency Climate Change Initiative (ESA CCI) soil moisture integrating satellite  
645 observations, model-driven knowledge, and spatiotemporal machine learning. *Hydrology*  
646 and *Earth System Sciences*, 27(2), 577–598. <https://doi.org/10.5194/hess-27-577-2023>
- 647 Lunch, C., Laney, C., Mietkiewicz, N., Sokol, E., Cawley, K., & NEON (National Ecological  
648 Observatory Network). (2025). *neonUtilities: Utilities for working with NEON data*. <https://doi.org/10.32614/CRAN.package.neonUtilities>
- 650 Luo, Y., Ogle, K., Tucker, C., Fei, S., Gao, C., LaDeau, S., Clark, J. S., & Schimel, D. S. (2011).  
651 Ecological forecasting and data assimilation in a data-rich era. *Ecological Applications*,  
652 21(5), 1429–1442. <https://doi.org/10.1890/09-1275.1>
- 653 Maier, M., & Schack-Kirchner, H. (2014). Using the gradient method to determine soil gas  
654 flux: A review. *Agricultural and Forest Meteorology*, 192–193, 78–95. <https://doi.org/10.1016/j.agrformet.2014.03.006>
- 656 Mariethoz, G., Linde, N., Jougnot, D., & Rezaee, H. (2015). Feature-preserving interpolation  
657 and filtering of environmental time series. *Environmental Modelling & Software*, 72, 71–76.  
658 <https://doi.org/10.1016/j.envsoft.2015.07.001>
- 659 Marshall, T. J. (1959). The Diffusion of Gases Through Porous Media. *Journal of Soil Science*,  
660 10(1), 79–82. <https://doi.org/10.1111/j.1365-2389.1959.tb00667.x>

- 661 Millington, R. J., & Shearer, R. C. (1971). Diffusion in aggregated porous media. *Soil Science*,  
662 111(6), 372–378.
- 663 Moffat, A. M., Papale, D., Reichstein, M., Hollinger, D. Y., Richardson, A. D., Barr, A. G.,  
664 Beckstein, C., Braswell, B. H., Churkina, G., Desai, A. R., Falge, E., Gove, J. H., Heimann,  
665 M., Hui, D., Jarvis, A. J., Kattge, J., Noormets, A., & Stauch, V. J. (2007). Comprehensive  
666 comparison of gap-filling techniques for eddy covariance net carbon fluxes. *Agricultural and  
667 Forest Meteorology*, 147(3), 209–232. <https://doi.org/10.1016/j.agrformet.2007.08.011>
- 668 Moldrup, P., Olesen, T., Yamaguchi, T., Schjønning, P., & Rolston, D. E. (1999). Modeling  
669 diffusion and reaction in soils: 9. The Buckingham-Burdine-Campbell equation for gas  
670 diffusivity in undisturbed soil. *Soil Science*, 164(2), 75.
- 671 National Ecological Observatory Network (NEON). (2024a). *Barometric pressure  
672 (DP1.00004.001)*. National Ecological Observatory Network (NEON). <https://doi.org/10.48443/RT4V-KZ04>
- 673
- 674 National Ecological Observatory Network (NEON). (2024b). *Soil CO<sub>2</sub> concen-  
675 tration (DP1.00095.001)*. National Ecological Observatory Network (NEON).  
676 <https://doi.org/10.48443/E7GR-6G94>
- 677 National Ecological Observatory Network (NEON). (2024c). *Soil physical and chemical prop-  
678 erties, Megapit (DP1.00096.001)*. National Ecological Observatory Network (NEON).  
679 <https://doi.org/10.48443/S6ND-Q840>
- 680 National Ecological Observatory Network (NEON). (2024d). *Soil temperature (DP1.00041.001)*.  
681 National Ecological Observatory Network (NEON). <https://doi.org/10.48443/Q24X-PW21>
- 682 National Ecological Observatory Network (NEON). (2024e). *Soil water content and water  
683 salinity (DP1.00094.001)*. National Ecological Observatory Network (NEON). <https://doi.org/10.48443/A8VY-Y813>
- 684
- 685 Norman, J. M., Kucharik, C. J., Gower, S. T., Baldocchi, D. D., Crill, P. M., Rayment,  
686 M., Savage, K., & Striegl, R. G. (1997). A comparison of six methods for measuring

- 687 soil-surface carbon dioxide fluxes. *Journal of Geophysical Research: Atmospheres*, 102(D24),  
688 28771–28777. <https://doi.org/10.1029/97JD01440>
- 689 Phillips, C. L., Bond-Lamberty, B., Desai, A. R., Lavoie, M., Risk, D., Tang, J., Todd-Brown,  
690 K., & Vargas, R. (2017). The value of soil respiration measurements for interpreting and  
691 modeling terrestrial carbon cycling. *Plant and Soil*, 413(1), 1–25. <https://doi.org/10.1007/s11104-016-3084-x>
- 693 Raftery, A. E., Gneiting, T., Balabdaoui, F., & Polakowski, M. (2005). *Using Bayesian Model  
694 Averaging to Calibrate Forecast Ensembles*. <https://doi.org/10.1175/MWR2906.1>
- 695 Sallam, A., Jury, W. A., & Letey, J. (1984). Measurement of Gas Diffusion Coefficient under  
696 Relatively Low Air-filled Porosity. *Soil Science Society of America Journal*, 48(1), 3–6.  
697 <https://doi.org/10.2136/sssaj1984.03615995004800010001x>
- 698 Shao, J., Zhou, X., Luo, Y., Li, B., Aurela, M., Billesbach, D., Blanken, P. D., Bracho, R.,  
699 Chen, J., Fischer, M., Fu, Y., Gu, L., Han, S., He, Y., Kolb, T., Li, Y., Nagy, Z., Niu, S.,  
700 Oechel, W. C., ... Zhang, J. (2015). Biotic and climatic controls on interannual variability  
701 in carbon fluxes across terrestrial ecosystems. *Agricultural and Forest Meteorology*, 205,  
702 11–22. <https://doi.org/10.1016/j.agrformet.2015.02.007>
- 703 Shao, P., Zeng, X., Moore, D. J. P., & Zeng, X. (2013). Soil microbial respiration from  
704 observations and Earth System Models. *Environmental Research Letters*, 8(3), 034034.  
705 <https://doi.org/10.1088/1748-9326/8/3/034034>
- 706 Sihi, D., Gerber, S., Inglett, P. W., & Inglett, K. S. (2016). Comparing models of microbial–  
707 substrate interactions and their response to warming. *Biogeosciences*, 13(6), 1733–1752.  
708 <https://doi.org/10.5194/bg-13-1733-2016>
- 709 Tang, J., Baldocchi, D. D., Qi, Y., & Xu, L. (2003). Assessing soil CO<sub>2</sub> efflux using continuous  
710 measurements of CO<sub>2</sub> profiles in soils with small solid-state sensors. *Agricultural and Forest  
711 Meteorology*, 118(3), 207–220. [https://doi.org/10.1016/S0168-1923\(03\)00112-6](https://doi.org/10.1016/S0168-1923(03)00112-6)
- 712 Tang, J., Misson, L., Gershenson, A., Cheng, W., & Goldstein, A. H. (2005). Continuous

- 713 measurements of soil respiration with and without roots in a ponderosa pine plantation  
714 in the Sierra Nevada Mountains. *Agricultural and Forest Meteorology*, 132(3), 212–227.  
715 <https://doi.org/10.1016/j.agrformet.2005.07.011>
- 716 Taylor, J. R. (2022). *An Introduction to Error Analysis: The Study of Uncertainties in Physical*  
717 *Measurements, Third Edition* (3rd ed.). University Science Press.
- 718 Yan, Z., Bond-Lamberty, B., Todd-Brown, K. E., Bailey, V. L., Li, S., Liu, C., & Liu, C. (2018).  
719 A moisture function of soil heterotrophic respiration that incorporates microscale processes.  
720 *Nature Communications*, 9(1), 2562. <https://doi.org/10.1038/s41467-018-04971-6>
- 721 Yan, Z., Liu, C., Todd-Brown, K. E., Liu, Y., Bond-Lamberty, B., & Bailey, V. L. (2016).  
722 Pore-scale investigation on the response of heterotrophic respiration to moisture conditions  
723 in heterogeneous soils. *Biogeochemistry*, 131(1), 121–134. <https://doi.org/10.1007/s10533-016-0270-0>
- 725 Zhang, R., Kim, S., Kim, H., Fang, B., Sharma, A., & Lakshmi, V. (2023). Temporal Gap-Filling  
726 of 12-Hourly SMAP Soil Moisture Over the CONUS Using Water Balance Budgeting. *Water*  
727 *Resources Research*, 59(12), e2023WR034457. <https://doi.org/10.1029/2023WR034457>
- 728 Zobitz, J., Ayres, E., O'Rourke, K., Werbin, Z., Lee, L., Abdi, R., Mehmeti, D., & Xiong, L.  
729 (2024). *neonSoilFlux: Compute Soil Carbon Fluxes for the National Ecological Observatory*  
730 *Network Sites*. <https://doi.org/10.32614/CRAN.package.neonSoilFlux>